AIAA 99-0181

Toward an Integrated Optical Data System for Wind Tunnel Testing

Wim Ruyten
Sverdrup Technology, Inc., AEDC Group
Arnold Engineering Development Center
Arnold Air Force Base, Tennessee 37389-4300

37th AIAA Aerospace Sciences Meeting & Exhibit
January 11-14, 1999 / Reno, NV

AIAA-99-0181

TOWARD AN INTEGRATED OPTICAL DATA SYSTEM FOR WIND TUNNEL TESTING*

Wim Ruyten†
Sverdrup Technology, Inc., AEDC Group
Arnold AFB, TN 37389-4300

Abstract

The question is addressed how registration markers in luminescent paint images can be used to determine model position and attitude (P&A) of the test article in a wind tunnel test. The theory for such P&A determinations is developed and applied to data from a recent pressure-sensitive paint test in AEDC's 16-ft transonic wind tunnel. It is shown that the camera system is capable of resolving pitch and yaw angles to within 0.005 deg rms. However, systematic differences as large as ±0.05 deg are found between the camera-based angles and angles determined from a sting-mounted balance. By analyzing the motion of the cameras relative to the tunnel walls, it is shown that the observed discrepancies may be explained by rotation of the cameras relative to the test article. In some cases, these rotations are clearly correlated to operating conditions of the tunnel. In the course of performing a sensitivity study, it is demonstrated that the mapping of 2D image data to a 3D grid can be improved by using the 2D image data to fine-tune the 3D model coordinates of the registration markers, which are obtained by a digitizing measurement arm.

1.0 Introduction

Luminescent paint measurements are assuming an increasingly prominent role in aerodynamic testing.[1-3] This is especially true at the Arnold Engineering Development Center, which is in the process of upgrading its pressure-sensitive paint (PSP) system for the 16-ft transonic wind tunnel to one that will employ eight cameras in the test section (see Fig. 1). To perform PSP measurements, a luminescent coating, whose luminescent yield under suitable illumination is a function of the pressure or temperature at the surface, is applied to a test article. By imaging the surface, it is thus possible to determine the pressure or temperature distribution on the test article. Most importantly, the PSP system is expected to reduce cycle time for test and development projects by providing faster and more comprehensive data than can be obtained by traditional techniques.

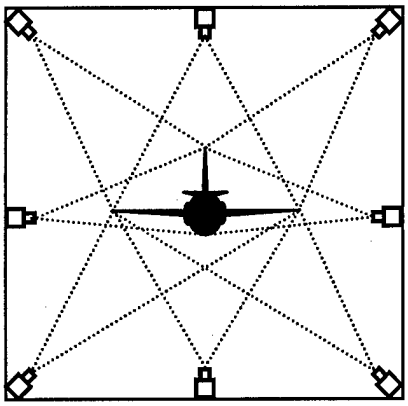

Fig. 1. Schematic of eight-camera PSP system for AEDC's 16-ft transonic wind tunnel.

A common task in luminescent paint measurements is resection.[4-6] This is the process of mapping two-dimensional (2D) image data onto a three-dimensional (3D) grid of the test article. To accomplish this task, registration markers are placed on the test article. The desired mapping transformations are then inferred from the coordinates of these markers in 3D object space and in 2D image space. This process presents the interesting opportunity to use the image coordinates of the registration markers to calculate the position and attitude (P&A) of the test article optically. By contrast, traditional measurements of model attitude involve a complex procedure for combining and calibrating data from sting-mounted balance sensors and strain gages. The accuracy of such measurements is estimated to be in the range 0.02 to 0.05 deg. The motivation for the present study was to investigate the possibility of using the optical data system

* *The research reported herein was performed by the Arnold Engineering Development Center (AEDC), Air Force Materiel Command. Work and analysis for this research were performed by personnel of Sverdrup Technology, Inc., AEDC Group, technical services contractor for AEDC. Further reproduction is authorized to satisfy needs of the U. S. Government.*

† Senior Engineer, Instrumentation and Diagnostics Branch; Member, AIAA.

to improve these accuracies to 0.01 deg or better, thereby meeting the level of accuracy desired more and more frequently by AEDC test customers.

The organization of this paper is as follows. In Section 2, principles of optical P&A determination are formulated for the problem at hand. In Section 3, these principles are applied to image data from three cameras that were used in a recent PSP test. In Section 4, the experimental findings from Section 3 are supplemented by sensitivity studies. Section 5 concludes with a discussion and a comparison of the results achieved at AEDC with optical data obtained in wind tunnels elsewhere.[6-9]

2.0 Theory

Determination of model P&A parameters by optical means is a well-known problem in photogrammetry.[9,10] Consider the process of imaging a test article ("the model") on which are placed a number of registration markers. Let (X_i,Y_i,Z_i) be the 3D coordinates of these markers in a coordinate system that is tied to the model, and let (u_i,v_i) be the corresponding 2D image coordinates. If lens distortion is neglected, the relation between these two sets of coordinates may be expressed as:[4,10,11]

$$u_i = \frac{b_1 X_i + b_2 Y_i + b_3 Z_i + b_4}{b_9 X_i + b_{10} Y_i + b_{11} Z_i + 1}, \tag{1a}$$

$$v_i = \frac{b_5 X_i + b_6 Y_i + b_7 Z_i + b_8}{b_9 X_i + b_{10} Y_i + b_{11} Z_i + 1}, \tag{1b}$$

where $b_1...b_{11}$ are camera calibration coefficients. Equations (1) may be interpreted either as a direct linear transform or as a projective transform. In the first case, $b_1...b_{11}$ are treated as independent parameters. In the second case, $b_1...b_{11}$ are constrained by the interior and exterior coordinates of the camera.[9,10] In both cases, the coefficients $b_1...b_{11}$ may be obtained by fitting measured values of the image coordinates (u_i,v_i) to a known set of model coordinates (X_i,Y_i,Z_i). This is the standard approach for performing resection in luminescent paint measurements. While adequate for mapping 2D image data onto a 3D grid, the resulting coefficients $b_1...b_{11}$ provide little insight into the position and attitude parameters of the test article, even though they depend on them.

In the alternative scheme considered here, a third coordinate system is introduced, namely that associated with the wind tunnel (see Fig. 2). With respect to the wind tunnel system, let the position of a reference point on the test article (for example, the center of mass — CM) be given by (x_0,y_0,z_0), and let the attitude of the test article be given by the three Euler angles α (pitch), β (yaw), and γ (roll). The relationship between the model coordinates (X_i,Y_i,Z_i) of a registration marker and the associated tunnel coordinates (x_i,y_i,z_i) is then given by

$$\begin{pmatrix} x_i \\ y_i \\ z_i \end{pmatrix} = \begin{pmatrix} x_0 \\ y_0 \\ z_0 \end{pmatrix} + \begin{pmatrix} R_{11} & R_{12} & R_{13} \\ R_{21} & R_{22} & R_{23} \\ R_{31} & R_{32} & R_{33} \end{pmatrix} \begin{pmatrix} X_i \\ Y_i \\ Z_i \end{pmatrix}, \tag{2}$$

where[12]

$$R_{11} = \cos\alpha\cos\beta, \tag{3a}$$
$$R_{12} = -\sin\beta\cos\gamma - \sin\alpha\cos\beta\sin\gamma, \tag{3b}$$
$$R_{13} = \sin\beta\sin\gamma - \sin\alpha\cos\beta\cos\gamma, \tag{3c}$$
$$R_{21} = \cos\alpha\sin\beta, \tag{3d}$$
$$R_{22} = \cos\beta\cos\gamma - \sin\alpha\sin\beta\sin\gamma, \tag{3e}$$
$$R_{23} = -\cos\beta\sin\gamma - \sin\alpha\sin\beta\cos\gamma, \tag{3f}$$
$$R_{31} = \sin\alpha, \tag{3g}$$
$$R_{32} = \cos\alpha\sin\gamma, \tag{3h}$$
$$R_{33} = \cos\alpha\cos\gamma. \tag{3i}$$

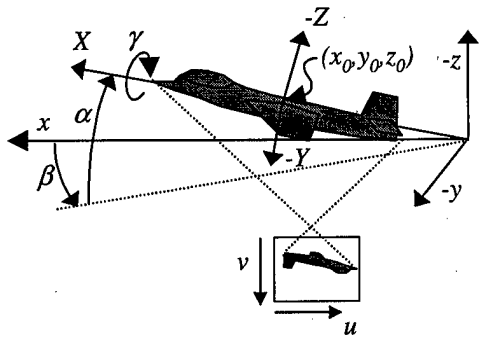

Fig 2. Definition of coordinate systems.

Now reinterpret the imaging equations from Eqs. (1) in terms of the tunnel coordinates (x_i,y_i,z_i). The P&A-dependent coefficients $b_1...b_{11}$ are replaced by the fixed coefficients $a_{1c}...a_{11c}$. The subscript "c" indicates that each camera has its own set of calibration coefficients. We can now write Eqs. (1) as

$$u_{ic} = U_{ic}/W_{ic}; \quad v_{ic} = V_{ic}/W_{ic}, \tag{4}$$

where

$$U_{ic} = a_{1c}x_i + a_{2c}y_i + a_{3c}z_i + a_{4c}, \tag{5a}$$
$$V_{ic} = a_{5c}x_i + a_{6c}y_i + a_{7c}z_i + a_{8c}, \tag{5b}$$
$$W_{ic} = a_{9c}x_i + a_{10c}y_i + a_{11c}z_i + 1. \tag{5c}$$

By combining Eqs. (2)-(5), an explicit expression is obtained for the image coordinates (u_i,v_i) in terms of the model coordinates (X_i,Y_i,Z_i), the camera calibration coefficients $a_{1c}...a_{11c}$, and the model P&A parameters x_0, y_0, z_0, α, β, and γ. Given the image coordinates of a sufficiently large set of markers, it is possible to determine the unknown parameters by minimizing the least-squares sum

$$Q = \sum_{i,c} \left\{ (u_{ic} - u_{ic}')^2 + (v_{ic} - v_{ic}')^2 \right\}, \qquad (6)$$

where the primed quantities are the measured image coordinates. As indicated, the sum in Eq. (6) may include image coordinates from multiple cameras. The model coordinates (X_i, Y_i, Z_i) are presumed known, in this case, through the use of a digitizing measurement arm. Minimization of Eq. (6) may thus be used either for calibrating the camera coefficients $a_{1c}...a_{11c}$ for a known set of model P&A parameters, or for determining model P&A parameters once the coefficients $a_{1c}...a_{11c}$ are known. In both cases, minimization of Q requires an iterative algorithm. A simplex algorithm[13] was used in this work. Starting values for the fit parameters were obtained by first minimizing the error sum

$$Q' = \sum_{i,c} \left\{ (U_{ic} - u_{ic}' W_{ic})^2 + (V_{ic} - v_{ic}' W_{ic})^2 \right\}, \qquad (7)$$

which is obtained from Eq. (6) by multiplying the terms in parentheses by the terms W_{ic}. Substituting the results from Eqs. (2) and (5) into Eq. (7) yields an expression for Q' that is quadratic in the camera coefficients $a_{1c}...a_{11c}$, in the model position parameters (x_0, y_0, z_0), and in the nine elements $R_{11}...R_{33}$ of the test-article rotation matrix. Setting to zero the derivatives of this expanded form of Eq. (7) with respect to the unknown parameters leads to a system of linear equations from which may be found, in the case of camera calibration, the coefficients $a_{1c}...a_{11c}$ (by solving 11 equations) or, in the case of model P&A determination, the 12 P&A parameters from Eq. (2) (by solving 12 equations). At least six coordinate pairs (u_{ic}', v_{ic}') are required in either case for these equations to have a unique solution. From these parameters, starting values for the iterative minimization of Eq. (6) may be constructed.

Figure 3 shows a flow chart of the resulting fitting processes. Camera calibration and model P&A determination are shown as separate processes. Both involve a linear step to obtain starting values for the fit parameters and an iterative step for their optimization. In all cases, the pre-eminent measure for the quality of the resulting fits is the rms deviation between fitted and measured image coordinates given by

$$\Delta_{rms} = (Q / N_{tot})^{1/2}, \qquad (8)$$

where N_{tot} is the total number of image coordinate pairs in the sum Q from Eq. (6).

The P&A determination technique described here differs from techniques used in stereo-photogrammetry in that it is not necessary to obtain explicit values for the tunnel coordinates (x_i, y_i, z_i) of the registration markers. The technique can be used with a single camera and offers the opportunity to combine measurements from multiple cameras even if their fields of view do not overlap. These

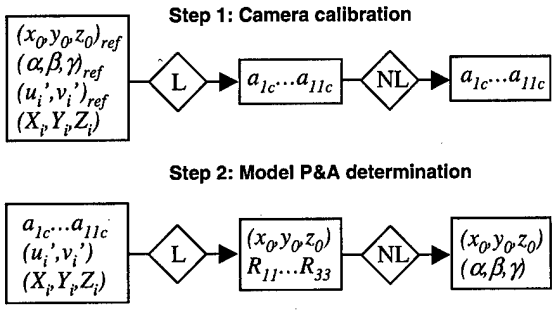

L=linear (direct) fit; NL=nonlinear (iterative) fit

Fig. 3. Processing steps.

advantages derive from the fact the relative locations of the registration markers are know through the use of a digitizing measurement arm.

3.0 Application to Wind Tunnel Data

The theory from Section 2 is now applied to image data from a recent PSP test in AEDC's 16-ft transonic tunnel. The test was performed on a 1:10 scale model of a German Dornier Alpha jet, known as the TST model.[14,15] Nominal pitch angles in the test were 0, 2, 4, 5, and 6 deg. No intentional yaw or roll angles were introduced. Only the right half of the model was painted. Three 1024 × 1024 × 16-bit CCD cameras were used: One ("*cam1*") mounted above the model, one ("*cam2*") mounted to the side of the model, and one ("*cam3*") mounted below the model. Figure 4 shows representative images from the test. Registration marks and image sizes, in pixels, are indicated. Camera focal lengths were in the range 50-60 mm, with aperture settings of f/8. Image exposure times were in the range 1-3 sec.

Forty-two registration markers were placed on the model. Ten of these were used in conjunction with the side-mounted camera; sixteen each were used in conjunction with the top- and bottom-mounted cameras. The registration markers consisted of black, circular dots, with diameters of 6.4 mm in model space, or about five image pixels in image space for all three cameras. Figure 5 shows a typical close-up view of a set of markers from the side-mounted camera.

A total of 344 images was used for P&A analysis: 90 for the side-mounted camera, 127 each for the top- and bottom-mounted cameras. Image coordinates of the registration markers were extracted from a database file, which was previously generated by the PSP analysis program. Analysis of the data was focused on two tasks: Determination of pitch angles from the side-mounted camera, and determination of yaw angles from, separately, the top- and bottom-mounted cameras. Traditional values for pitch, yaw, and roll of the model were also available from digital angle sensors and strain gages on a sting-mounted balance. These angles include corrections for

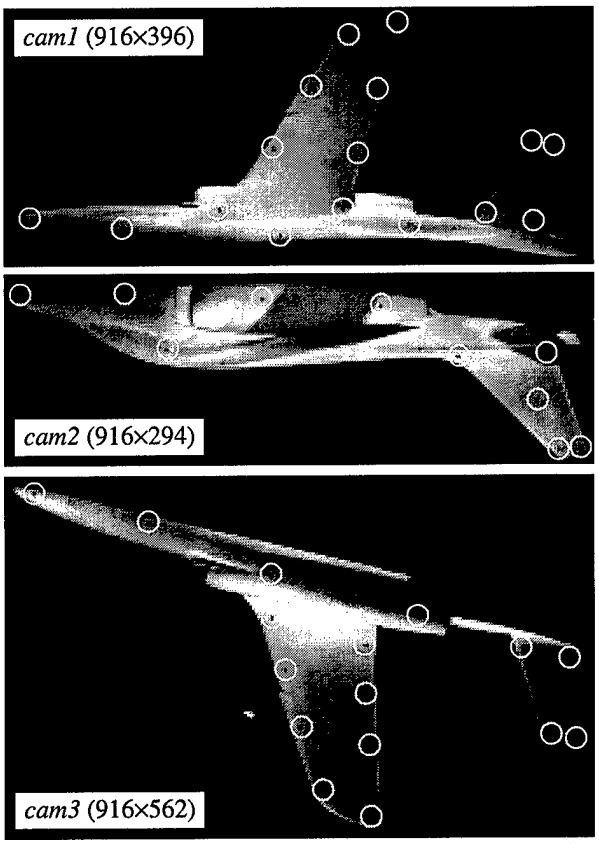

Fig. 4. PSP images of TST model at wind-off test point 16301.

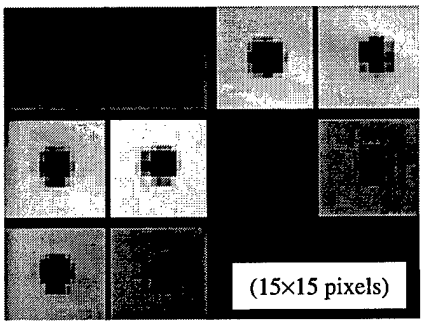

Fig. 5. Close-up view of *cam2* registration markers from Fig. 4.

sting deflections under dynamic loading, and are believed to be accurate to about 0.02-0.03 deg. All pitch angles quoted here exclude a Mach-number-dependent flow-angle correction (a number in the range 0 to –0.26 deg), which cannot be measured optically. No flow-angle corrections were considered for yaw.

3.1 Definition of Tunnel Coordinate System

To define the tunnel coordinate system *xyz* from Fig. 2, it was assumed in essence that, at a reported pitch angle of 0 deg, the tunnel axes *xyz* are aligned with the model axes *XYZ* of the TST model. In turn, the model *XYZ* coordinates were determined in four steps. First, the TST model was positioned at 0-deg pitch, yaw, and roll. Second, to calibrate the digitizing measurement arm, the tip of the arm was placed on selected pressure taps whose 3D coordinates were assumed to be those from an engineering drawing of the TST model. Third, having established a coordinate system for the measurement arm in this way, the *XYZ* model coordinates of the registration markers on the top of the model and the fuselage were measured. Fourth, to access the markers on the bottom of the model, the model was rolled over 180 deg and the second and third steps were repeated.

3.2 Data Analysis

Model position and attitude of the TST model were determined from the PSP images by following the two processes from Fig. 3. Projective transform equations were used both for camera calibration and P&A determination. Camera calibration coefficients $a_{1c}...a_{11c}$ were determined for each camera separately. The wind-off test point 16301, at a reported pitch angle of –0.09 deg, was selected as a reference. Yaw and roll angles for this point were taken to be 0 deg by definition. Likewise, the position of the CM of the model, (x_0,y_0,z_0), was defined to be $(0,0,0)$ at this point. The tunnel coordinates (x_i,y_i,z_i) of all 42 registration markers could thus be calculated using Eqs. (2) and (3). The camera coefficients $a_{1c}...a_{11c}$ were then found separately for each camera by successive minimization of Eqs. (7) and (6), using as input the image coordinates of the registration markers from the three images in Fig. 4.

After obtaining the camera calibration coefficients $a_{1c}...a_{11c}$, model P&A parameters were determined for all images, including those at the reference point 16301. For each image, successive minimization of Eqs. (7) and (6) yielded three position parameters for the CM, as well as values for pitch, yaw, and roll of the model. Typical values for the residual fit errors from Eq. (8) were 0.21 pixels rms for *cam1*, 0.12 pixels rms for *cam2*, and 0.45 pixels rms for *cam3*.

3.3 Pitch Angle Results

Image data from the side-mounted camera (*cam2*) were used to calculate model pitch. The results are plotted in Fig. 6 as a function of image sequence number. In this format, the data merely reveal the 0- to 6-deg range of pitch angles used in the test. To assess the accuracy of the data, Fig. 6 also shows the differences between the camera-based pitch angles and the pitch angles that were derived from the wind tunnel balance. Differences in the range –0.06 to +0.06 deg are found, with an rms deviation of 0.028 deg from zero. The differences are surprisingly large and are clearly not randomly distributed. The big

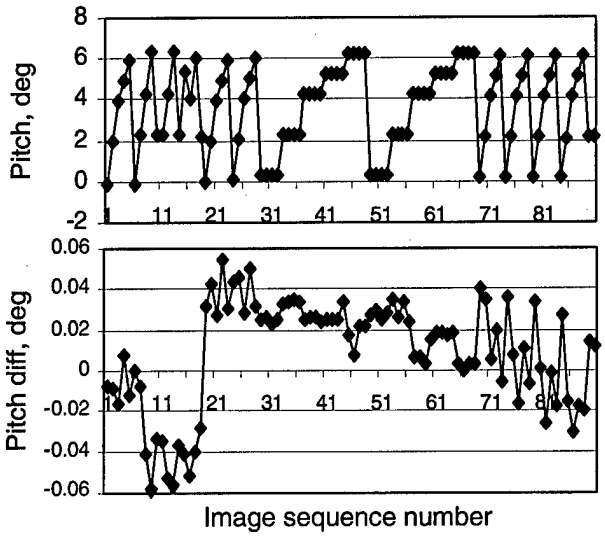

Fig. 6. History of pitch angles and pitch angle differences between *cam2* data and balance-derived values.

jump in pitch angle difference between the eighteenth and nineteenth data points coincides with a change from a wind-on condition to wind-off. During this process, an adjustment had to be made to the *cam2* camera. Thus, the large jump between the eighteenth and nineteenth data points may have been caused by bumping the camera. To check for this effect, the *cam2* images were reanalyzed to check for rotation of the camera relative to the tunnel wall in the background of the *cam2* images. As an example, Fig. 7 shows a greatly enhanced version of the *cam2* image at the reference test point, point 16301 (cf. Fig. 4). Figure 8 shows a detailed view of the features (mostly holes in the perforated wall) that were selected to serve as registration markers. The image centroids of these features were calculated for all of the *cam2* images. For each image separately, the centroids were then fitted to the expression

$$\begin{pmatrix}\Delta u_i\\ \Delta v_i\end{pmatrix}=\begin{pmatrix}\Delta u\\ \Delta v\end{pmatrix}+\begin{pmatrix}1 & -\delta\\ \delta & 1\end{pmatrix}\begin{pmatrix}u_i-u_c\\ v_i-v_c\end{pmatrix}, \qquad (9)$$

where Δu_i and Δv_i are the shifts in image coordinates of the ith feature in a given image relative to the reference image (at test point 16301), and u_i-u_c and v_i-v_c are the displacements of the image coordinates in the reference image from the image center. The three fit parameters in Eq. (9) are the image shifts Δu and Δv, and the image rotation angle δ, which is assumed to be small. Table 1 lists typical residual fit errors [cf. Eq. (8)] and image shifts, both in terms of image pixels and millimeter displacements relative to the tunnel wall. Most importantly, Fig. 9 shows the rotation angles δ as a function of image sequence number. Unmistakably, the same jump in pitch angle is found as that which is seen

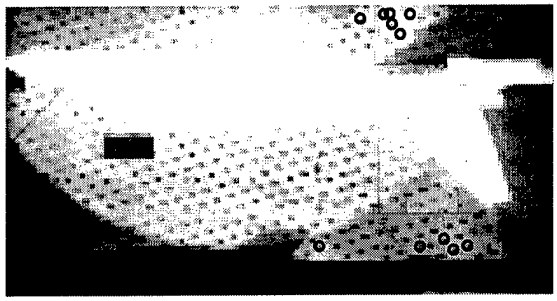

Fig. 7. View of tunnel wall opposite of *cam2* camera. Circles indicate image features used for camera-wall rotation analysis.

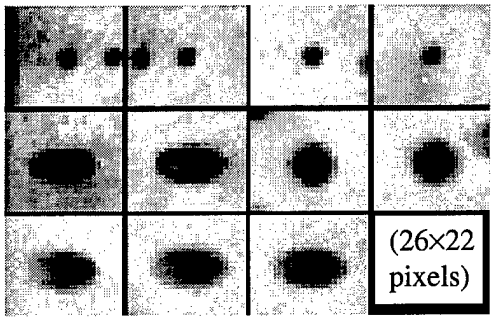

Fig. 8. Close-up view of *cam2* image features from Fig. 7.

between the eighteenth and nineteenth points in Fig. 6. This indicates that the discrepancy between the camera-based pitch angles in Fig. 6 and the balance-derived values is based, at least in part, on motion of the *cam2* camera.

Table 1. Wall-Camera Displacement Analysis for cam2

Number of Images	90
Number of Registration Features	11
Fit Error Δ_{rms}, pixels	0.15 to 0.25
Δu Range, pixels	0.5 to -4.5
Δv Range, pixels	0 to –2.5
Δu Range, mm on wall	-2 to -12
Δv Range, mm on wall	0 to -7

Apart from the big jump between points 18 and 19, the rotation angles in Fig. 9 show a distinct correlation to tunnel Mach number, which is also shown in Fig. 9. Four of the five changes in Mach number are clearly reflected in the camera-to-wall rotation data. This does not imply that only the camera moves. As will be seen in Section 3.3, it is in fact likely that the tunnel walls move as well. The rotation effect in Fig. 9 is thus likely a composite effect of camera motion and wall motion. As a result, the rotation angles from Fig. 9 do not necessarily account for all of the observed discrepancies between the *cam2*-based pitch angles and the balance-derived values in Fig. 6.

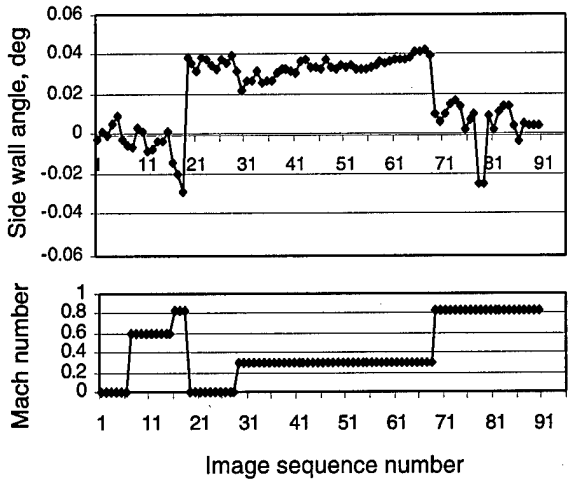

Fig. 9. History of observed wall rotation angles as seen by *cam2*, alongside tunnel Mach number.

3.4 Yaw Angle Results

No deliberate yaw angles were introduced in the TST test. Still, the procedures from Section 2 were followed to determine yaw angles for both the top- and bottom-mounted cameras. The results are shown in Fig. 10, which shows histories of the *cam1*- and *cam3*-derived yaw angles for all of the 127 test points for which both *cam1* and *cam3* images were available. Angles in the range 0-0.1 deg are found. The direction of yaw is "nose to the left", or right wing swept forward, relative to the wind-off reference test point, point 16301. The observed yaw angles correlate strongly with model pitch, which is shown in the bottom of Fig. 10. Figure 11 shows this correlation explicitly for the wind-off data from Fig. 10.

A linear dependence of yaw versus pitch is found for both cameras. This indicates that the true pitch axis of the tunnel is rolled with respect to the *y*-axis of the assumed tunnel coordinate system in Fig. 2 by an angle whose tangent is given by the slope of the curve fits. Actually, different roll misalignment angles are found for the two cameras, namely 0.50 deg for *cam1* and 0.36 deg for *cam3*. Apparently, this discrepancy traces back to the fact that two orientations of the TST model were used (see Section 3.2) to measure the *XYZ* model coordinates of all 42 registration markers. The data from Fig. 11 thus imply that the model coordinates of the markers on the top of the model (those imaged by *cam1*) are rolled relative to the bottom markers (those imaged by *cam3*) by the difference of the two misalignment angles, that is, by 0.14 deg. In addition, Fig. 11 suggests that the model may have been mounted at a roll angle in the range 0.36 to 0.50 deg relative to the true pitch axis of the wind tunnel.

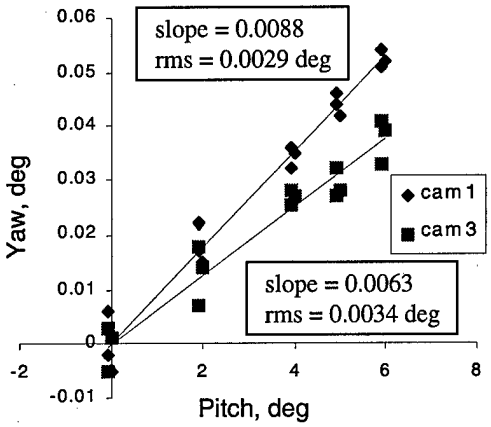

Fig. 11. Yaw versus pitch for wind-off data.

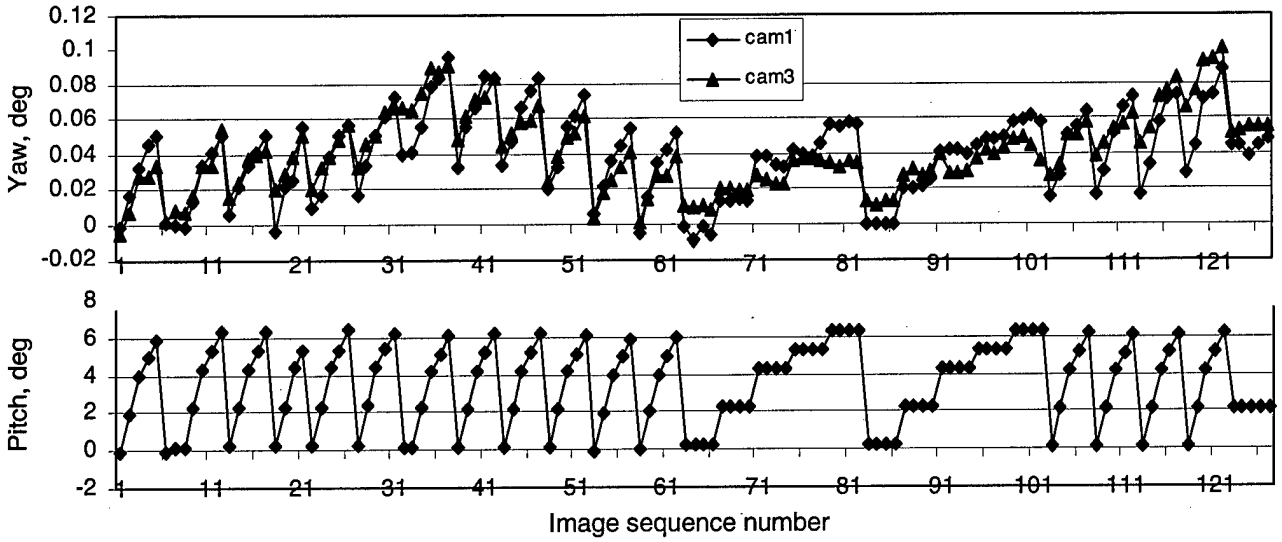

Fig. 10. Histories of observed yaw and pitch angles.

Figure 12 shows the yaw angles from Fig. 10, after removing the pitch-dependent component that is implied by the curve fits in Fig. 11. Angles in the range 0 to 0.06 deg remain. The corrected yaw angles correlate strongly to dynamic pressure ("*Q*"), which is shown in the bottom of Fig. 12. Such Q-dependent yaw effect would not be implausible in the presence of a sufficient side force or yawing moment on the model. However, calculated yaw angles for the TST model based on the measured side forces and yawing moments are less than 0.01 deg! It thus appears that the yaw angles in Fig. 12 may have to be interpreted in terms of camera motion.

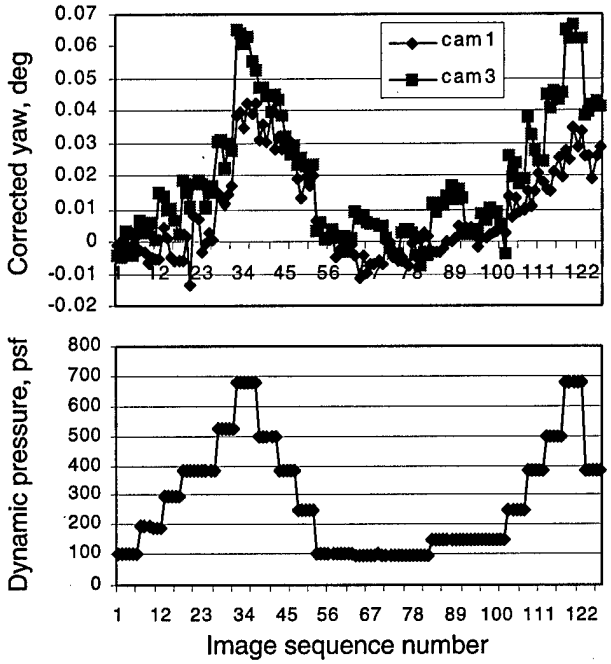

Fig. 12. Histories of pitch-corrected yaw and dynamic pressure.

To check for the existence of such camera motion, wall-to-camera rotation angles were calculated for all of the *cam1* and *cam3* images, using the procedure described in Section 3.3. Figure 13 shows the views of the bottom and top walls, with the registration features marked that were used for the analysis. Table 2 summarizes the fit results in the format from Table 1. Camera-to-wall rotation angles for both *cam1* and *cam3* are shown in Fig. 14. The two sets of data are almost identical, with an rms difference of only 0.007 deg. In addition, the camera-to-wall rotation angles in Fig. 14 are matched almost perfectly by the differences in the corrected model yaw angles from *cam1* and *cam3* in Fig. 12. Allowing for a constant offset of 0.014 deg, this difference angle agrees with the average of the *cam1* and *cam3* camera-to-wall rotation angles in Fig. 14 to 0.0072-deg rms. The following argument can now be made to prove that the

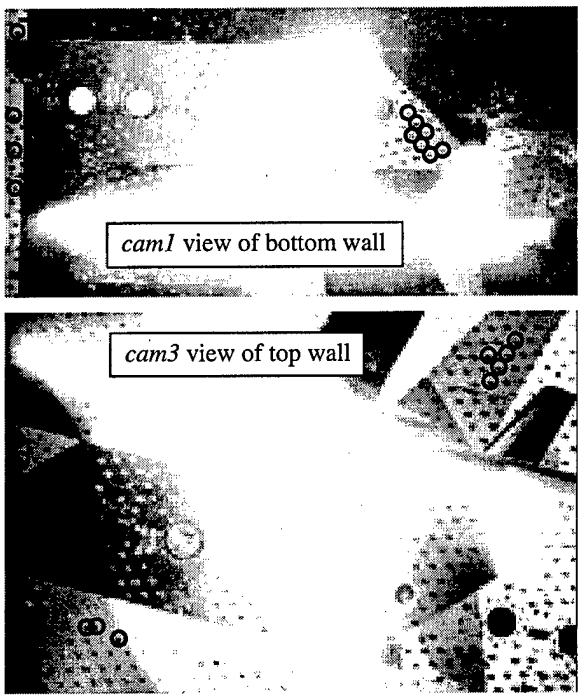

Fig. 13. Views of tunnel walls from top- and bottom-mounted cameras. Circles indicate image features used for camera-wall rotation analysis.

top tunnel wall is yawing with respect to the bottom wall. Let $\beta_{c1}(t)$ and $\beta_{c3}(t)$ be the time-dependent yaw angles of the top and bottom cameras, respectively, relative to a presumed absolute reference system. Likewise, let $\beta_{w1}(t)$ and $\beta_{w3}(t)$ be the time-dependent yaw angles of the top and bottom walls. Then the three sets of data in Fig. 14 may be thought of as defining the following three relationships between these angles:

$$\beta_{c1}(t) - \beta_{w3}(t) = f(t), \qquad (10a)$$

$$\beta_{w1}(t) - \beta_{c3}(t) = f(t), \qquad (10b)$$

$$\beta_{c1}(t) - \beta_{c3}(t) = f(t), \qquad (10c)$$

where $f(t)$ is the history of the three sets of data in Fig. 14. By combining Eqs.(10b) and (10c), it follows that $\beta_{c1}(t) = \beta_{w1}(t)$. That is, the top camera yaws at the same rate as the top wall. Likewise, by combining Eqs.(10a) and (10c), it follows that $\beta_{c3}(t) = \beta_{w3}(t)$. That is, the bottom camera yaws at the same rate as the bottom wall. Finally, by adding Eqs. (10a) and (10b) and subtracting Eq. (10c), it follows that $\beta_{w1}(t) - \beta_{w3}(t) = f(t)$. That is, the top wall and the bottom wall yaw relative to each other. Using also the fact that the model itself does not yaw (as follows from the force and moment data), it thus follows that the Q-dependent yaw effects in Fig. 12 are really those of the top and bottom walls of the tunnel, with the bottom wall displaying the largest amount of yaw. This effect is illustrated in Fig. 15.

Table 2. Results of Further Wall Displacement Analysis

	cam1	*cam3*
Number of Images	127	127
Number of Features	11	10
Fit Error Δ_{rms}, pixels	0.15-0.60*	0.15-0.25
Δu Range, pixels	0 to -4.5	-1.5 to 3
Δv Range, pixels	0 to -1	-0.5 to 2
Δu Range, mm on wall	0 to -12	-4 to 8
Δv Range, mm on wall	0 to -3	-1 to 5

*Residual fit errors can be reduced, without an appreciable change in the calculated rotation angles, to 0.22 pixels rms by including a thermal expansion coefficient for the flow direction.

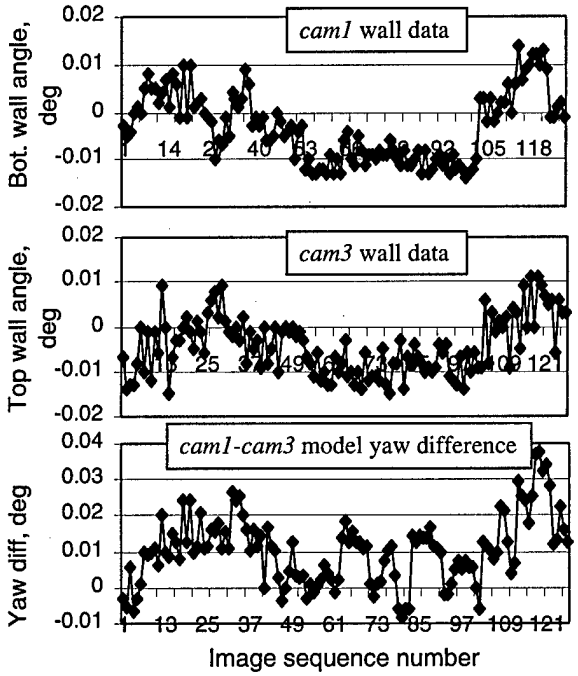

Fig. 14. Rotation angles for bottom and top tunnel walls, alongside model-based yaw-angle difference between top- and bottom-mounted cameras.

4.0 Sensitivity Studies

The results from Section 3 suggest that a more rigorous mounting scheme is desirable for the CCD cameras, if these are to be used for determining model pitch and yaw angles with an absolute accuracy of 0.01 deg or better. This will not be an easy task if the whole structure of the test cell flexes under dynamic and thermal loading, as is suggested by the data from Section 3. On the other hand, the data from Section 3 suggest that the sensitivity of the pitch- and yaw-angle determinations is on the order of 0.005 deg rms or better. For example, the residual fit errors in the yaw-versus-pitch curve fits from Fig. 11 are 0.0029 deg rms for the *cam1* data and 0.0034 deg rms for

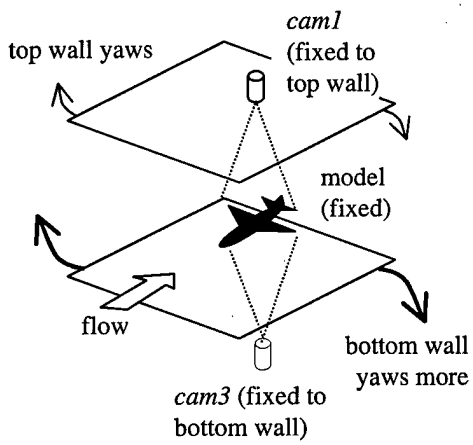

Fig. 15. Suggested mechanism for apparent model yaw with increasing dynamic pressure.

the *cam3* data. Also, the differences of 0.007 deg rms for the three sets of curves in Fig. 14 imply random errors in the individual rotation angle measurements of $0.007/\sqrt{2} = 0.005$ deg rms. Generally, 0.005 deg rms appears to be about the component of noise in most of the data from Section 3. It thus appears that, if the problems caused by camera motion can be resolved, absolute measurements of model yaw and pitch with an accuracy of better than 0.01 deg rms should be possible. To lend further support to this claim, two sources of error are examined in some detail. These are errors associated with the two sets of experimental data that are used as inputs to the model P&A determination process in Fig. 3. These two sets of data are the model coordinates (X_i, Y_i, Z_i) of the registration markers and the image coordinates (u_i, v_i) of said markers.

4.1 Errors in Model Coordinates

In Section 3.4 we have already encountered the effects of errors in model coordinates that may come about if not all registration markers on the model are accessible with a single initialization of the digitizing measurement arm. Errors in the model coordinates (X_i, Y_i, Z_i) can also come about due to intrinsic inaccuracies in the digitizing measurement arm and due to the difficulty of placing the measurement tip of the instrument precisely at the center of each registration marker. In the latter case, the measured point is on the model surface, but displaced from the actual marker centroid. Here we consider a procedure that may be used to correct for this type of measurement error. The central idea is that a 2D image of a marker constrains the possible locations of the marker to a ray in 3D space, and that intersecting this ray with the model surface yields the true 3D coordinates of the marker.

To put this idea into practice, let the three-vector $\mathbf{X}_i$ denote the true, unknown model coordinates of a registration marker and let $\mathbf{X}_i'$ denote the incorrectly measured coordinates of the marker. By assumption, $\mathbf{X}_i$ and $\mathbf{X}_i'$ are both located on the model surface. Neglecting curvature of the surface, the true position of the marker, $\mathbf{X}_i$, is thus given in terms of the incorrectly measured position, $\mathbf{X}_i'$, by

$$\mathbf{X}_i = \mathbf{X}_i' + \lambda_i \mathbf{l}_i + \mu_i \mathbf{m}_i , \qquad (11)$$

where $\mathbf{l}_i$ and $\mathbf{m}_i$ are unit tangential vectors on the surface (see Fig. 16). The true position of the marker, $\mathbf{X}_i$, may now be found by combining Eqs. (11) and (1), the latter of which defines the ray in Fig. 16 that is associated with the measured image coordinates (u_i, v_i) of the registration marker. The unknowns to be solved for are the parameters λ_i and μ_i. Once these are obtained, the true coordinates of the marker are given by Eq. (11).

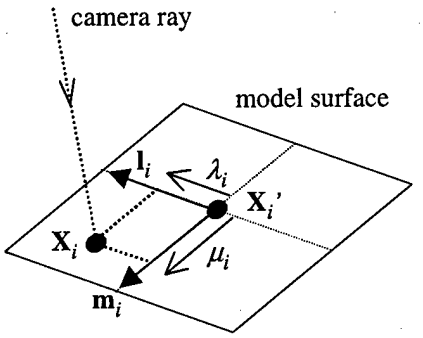

Fig. 16. Back-projection geometry for finding the actual marker position $\mathbf{X}_i$ from the measured marker position $\mathbf{X}_i'$.

This back-projection technique was used to recalculate the model coordinates (X_i, Y_i, Z_i) of all 42 registration markers on the TST model. First, tangential vectors $\mathbf{l}_i$ and $\mathbf{m}_i$ were calculated for each marker based on estimated surface normals. Second, for each image, the coefficients $b_1 \ldots b_{11}$ from Eqs. (1a-b) were calculated by performing a projective transform fit to the measured image coordinates. The uncorrected model coordinates (X_i, Y_i, Z_i) were used for this purpose. Third, also for each image, the back-projection parameters λ_i and μ_i were calculated for each marker. Finally, for each marker, average values of the parameters λ_i and μ_i were calculated, and improved coordinates of the registration markers were calculated using Eq. (11).

Figure 17 shows two examples of the "clouds" of back-projection parameters λ_i and μ_i that form around the original marker position (the origin in Fig. 17) in the third step of the back-projection process. For *cam1* marker #1, the cloud is wider than the displacement of the cloud from the origin. However, for *cam3* marker #43, the displacement is significant, indicating that the supplied

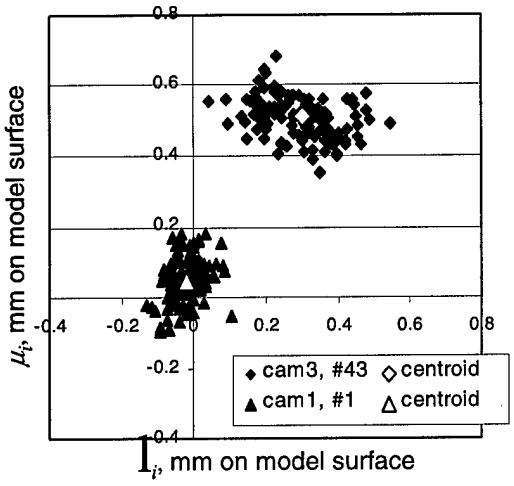

Fig. 17. Examples of back-projection distributions for two registration markers.

Table 3. Results of Back-Projection Corrections

	cam1	*cam2*	*cam3*
Number of Images	127	90	127
Number of Markers	16	10	16
Δs_{rms}, pix in image	0.16	0.09	0.35
Δs_{max}, pix in image	0.30	0.16	0.66
Δs_{rms}, mm on model	0.23	0.11	0.51
Δs_{max}, mm on model	0.43	0.21	0.95
Δ_{rms}, pix (w/o corr.)	0.21	0.12	0.45
Δ_{rms}, pix (with corr.)	0.09	0.08	0.09
$\Delta\alpha_{rms}$, deg	-	0.001	-
$\Delta\beta_{rms}$, deg	0.001	-	0.002

model coordinates of the marker are incompatible with its measured location in the images.

Table 3 groups the results of the back-projections by camera. On rows 3-6, rms and maximum displacements Δs are listed, both in terms of image pixels and distance on the model surface. The rms displacement on the surface is about equal to the quoted accuracy, 0.3 mm, of the digitizing measurement arm. Rows 7 and 8 list the average fit errors Δ_{rms} from Eq. (8), both without and with application of the back-projection corrections. The corrected fit errors were obtained by recalculating the projective transforms using the corrected model coordinates. This resulted in a lowering of the residual fit errors from 0.21 to 0.09 pixels rms for *cam1*; from 0.12 to 0.08 pixels rms for *cam2*; and from 0.45 to 0.09 pixels rms for *cam3*. As should be the case, these residual fit errors are nearly identical for the three cameras. No further lowering of the residual fit errors could be obtained by repeating the correction procedure on the corrected model coordinates. Using the corrected model coordinates, the model pitch and yaw calculations from Section 3 were repeated. The last two rows in Table 3 list

the amounts by which the resulting yaw and pitch angles differ from the values obtained in Section 3. The differences are only a few thousandths of a degree. That is, they are practically negligible! We thus see that the accuracy of the P&A determinations is not affected by small systematic errors in the measured model coordinates of the registration markers. This finding may be understood by noting that systematic errors in the model coordinates of the registration markers affect camera calibration and subsequent model P&A determination (the two processes in Fig. 3) in the same way. The correction procedure described here is thus not needed to improve the accuracy of P&A determinations. On the other hand, use of the corrected model coordinates should improve the accuracy of the resection process, whereby 2D image data are mapped onto a 3D grid.

4.2 Errors in Image Coordinates

We now consider a second source of error, namely that associated with finding the exact centers of individual registration markers in the CCD images. See Fig. 18, which shows a hypothetical, perfect image of a round marker on a smooth background, and the discrete image of this marker in the presence of signal noise. Let (u_i,v_i) be the centroid coordinates of the hypothetical image in Fig. 18a and let (u_i',v_i') be the centroid coordinates associated with the actual image in Fig. 18b. Then the errors in the measured image coordinates may be expressed as

$$\Delta u_i = u_i' - u_i; \quad \Delta v_i = v_i' - v_i . \tag{12}$$

Without inquiring into the detailed origins of the pixel shifts $(\Delta u_i,\Delta v_i)$, it is possible to study their effect on the resulting model P&A determinations by Monte Carlo simulation. For the pitch angle determinations from Section 3.3, this simulation was performed as follows.

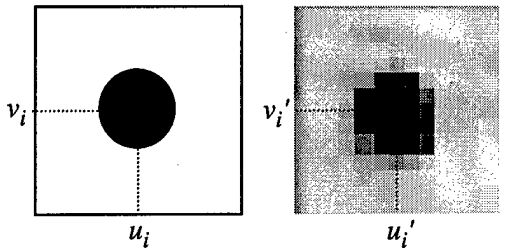

a. Idealized b. Actual

Fig. 18. Idealized and actual marker images.

First, an ideal set of image coordinates was calculated for the 10 registration markers associated with the *cam2* images. Model position and attitude were selected to be those of the reference test point in Section 3, point 16301, taken at a pitch angle of –0.09 deg. Second, idealized image coordinates for the *cam2* images were calculated using the camera calibration coefficients $a_{1c}...a_{11c}$ that were determined previously for the *cam2* image at the reference test point. Third, random shifts $(\Delta u_i,\Delta v_i)$ of known magnitude and direction were added to these coordinates, and model P&A parameters were calculated. This third step was repeated thousands of times. Fourth, ensemble averages of the resulting rms pitch angle errors and the associated fit errors Δ_{rms} from Eq. (8) were calculated. These quantities are plotted in Fig. 19 as a function of the rms magnitude of the applied image-coordinate shifts. In both cases, a linear dependence is found, with slopes as indicated in Fig. 19.

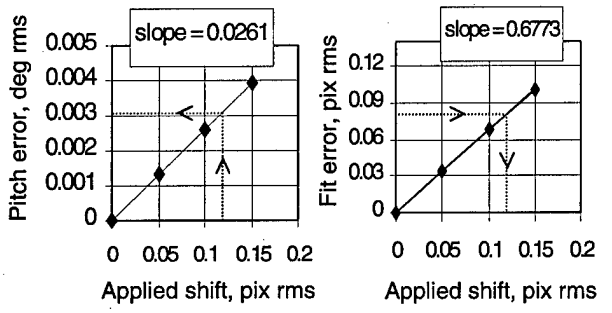

a. Pitch error b. Fit error

Fig. 19. Results of Monte Carlo simulation for pitch angle determinations.

It is now possible to estimate the random components of error in the pitch angle determinations from Section 3.3 in two steps. First, it is observed that the random component of residual fit error Δ_{rms} for the *cam2* images is 0.08 pixels. This is the value from row 8 in Table 3, that is, the residual fit error after back-projection correction of the supplied model coordinates of the registration markers. Inspection of Fig. 19b shows that such a residual fit error is obtained for an rms image coordinate shift of 0.08/0.6773 = 0.118 pixels rms. Second, Fig. 19a shows that the rms pitch angle error, $\Delta\alpha_{rms}$, that is associated with such an rms image coordinate shift is 0.118×0.0261 = 0.0031 deg rms. The calculation was repeated for a pitch angle of 6 deg, yielding identical results. It is thus concluded that the random component of error in the pitch angle determinations from Section 3.4 is 0.003 deg rms, independent of pitch angle. This value is consistent with the random scatter of the pitch angles in Figs. 6 and 9.

A similar Monte Carlo simulation was performed for the *cam1* yaw angle determinations from Section 3.4. Based on a random residual fit error of 0.09 pixels (see again row 8 in Table 3), the random component of yaw angle errors, $\Delta\beta_{rms}$, for the *cam1* yaw angle determinations was determined to be 0.005 deg rms. The same value was found for the *cam3* yaw angle determinations. Again, these values are consistent with the random scatter in the data from Section 3, specifically in Figs. 10, 11, 12, and 14.

4.3 Lens Distortion and Model Deformation

Two possible sources of error that have not been considered are lens distortion in the imaging optics and model deformation at wind-on test conditions relative to wind-off conditions. In the case of lens distortion, correction terms need to be added to the imaging equations from Eqs. (1) and (4).[9,10] These are accompanied by additional coefficients that need to be determined during the camera calibration process from Fig. 3. Likewise, in the case of model deformation, additional terms can be added to Eq. (2) to account for a nonlinear dependence of the wind-on tunnel coordinates of registration markers on their wind-off model coordinates. The associated deformation coefficients then become additional fit parameters during the model P&A determination step from Fig. 3.

The inclusion of both lens distortion effects and model deformation effects in the theory from Section 3 warrants further study. For the TST test from Section 3, both effects must have been small, judged by the fact that a single set of model coordinates exists (namely that found by performing the back-projection corrections on the model coordinates measured by the digitizing measurement arm) for which the linear equations from Section 3 fit the measured image coordinates to better than 0.1 pixels rms, regardless of pitch angle and tunnel operating conditions.

5.0 Discussion

The results from Sections 3 and 4 demonstrate that the CCD camera system that is used for performing PSP measurements in AEDC's 16-ft transonic wind tunnel can be used to measure model pitch and yaw angles with a sensitivity of about 0.003- to 0.005-deg rms. However, absolute accuracies for these measurements appear to be limited to about ±0.05 deg, due to apparent motion of the CCD cameras relative to the test article. Some of this camera motion may be the result of the fact that the mounting scheme for the cameras in the TST test was not designed with accurate model P&A determination in mind. However, the results indicate that some of the observed camera motion may be related to large-scale flexing of the test section. Such flexing may not be easy to resolve and would have equal impact on other optical attitude measurement systems. Independent measurements of camera motion (for example, through the use of gravity-sensing accelerometers) are desirable to resolve remaining ambiguities. Another possible approach to resolving such ambiguities is to perform redundancy checks among P&A measurements from multiple cameras. The eight-camera system that is being installed in AEDC's 16-ft transonic wind tunnel should offer several opportunities in this regard.

The sensitivities of 0.003- to 0.005-deg rms for pitch and yaw determinations compare favorably with numbers quoted by other researchers. For example, in Refs. 6-8, resolutions in the range "sub-0.01" to 0.05 deg are quoted for the measurement of wing twist by optical means. A direct comparison is difficult, as the results depend on a host of factors, including camera optics, marker size and placement, and data processing.

A subtle point uncovered in this study is the practical difficulty of aligning the camera coordinate systems to the coordinate systems of the wind tunnel. As demonstrated, yaw measurements during a pitch sweep may be used to calibrate roll angle misalignment of the tunnel pitch axis and the body *Y*-axis of the model. Likewise, roll measurements during a pitch sweep might be used to calibrate yaw angle misalignment of the pitch axis.

Further improvements that may be contemplated for the AEDC optical data system include the inclusion of lens distortion effects in the imaging equations, application of the technique to measurement of model deformation, and on-line data processing to provide position and attitude information in real time. Of course, P&A determinations are not limited to pressure-sensitive paint tests. Rather, they should be applicable in most cases in which it is possible to place registration markers on the surface of the test article.

A side product of this study that might find application for improving the mapping of luminescent paint image data onto a 3D grid is the back-projection procedure described in Section 4.1. As shown, this procedure may be used to fine-tune the *XYZ* model coordinates of the registration markers, relative to the coordinates supplied by a digitizing measurement arm.

Acknowledgements

Discussions with my colleagues Daryl Sinclair, Marvin Sellers, David Cahill, and Dr. Frank Steinle are greatly appreciated. The TST program was conducted under a Memorandum of Understanding between the United States Air Force (USAF) and the German Ministry of Education, Science, Research, and Technology (BMBF). Permission to publish images from the TST test was granted by Dr. Egon Stanewsky, for BMBF. The author also wishes to acknowledge discussions with Dr. Tianshu Liu of High Technology Corporation, Hampton, VA, for sharing insights into the applications of photogrammetry in wind tunnels.

References

1. Kavandi, J., et al., "Luminescent Barometry in Wind Tunnels," *Rev. Sci. Instrum.,* Vol. 61, 1990, pp. 3340-3347.

2. Morris, M. J., et al., "Aerodynamic Applications of Pressure Sensitive Paint," *AIAA J.*, Vol. 31, 1993, pp. 419-425.
3. McLachlan, B. G. and Bell, J. H., "Pressure-Sensitive Paint in Aerodynamic Testing," *Exp. Therm. and Fluid Science*, Vol. 10, 1995, pp. 470-485.
4. Bell, J. H. and McLachlan, B. G., "Image Registration for Luminescent Paint Sensors," AIAA Paper 93-0178, Reno, NV, January 1993. Also: Bell, J. H., and McLachlan, B. G., "Image Registration for Pressure-Sensitive Paint Applications," *Exp. in Fluids*, Vol. 22, 1996, pp. 78-86.
5. Le Sant, Y., Deleglise, B., and Mebarki, Y., "An Automatic Image Alignment Method Applied to Pressure Sensitive Paint Measurements," Proceedings of the 17th International Congress on Instrumentation in Aerospace Simulation Facilities, Pacific Grove, CA, Sep. 29-Oct. 2, 1997, Owen, F. K., Ed., pp. 57-65.
6. Bosnyakov, S., et al., "Blade Deformation and PSP Measurements on the Large Scale Rotor by Video Metric System," Proceedings of the 17th International Congress on Instrumentation in Aerospace Simulation Facilities, Pacific Grove, CA, Sep. 29-Oct. 2, 1997, Owen, F. K., Ed., pp. 95-103.
7. Bell, J. H. and Burner, A. W., "Data Fusion in Wind Tunnel Testing; Combined Paint and Model Deformation Measurements," AIAA Paper 98-2500, Albuquerque, NM, June 1998.
8. Burner, A. W. and Martinson, S. D., "Automated Wing Twist and Bending Measurements under Aerodynamic Load," AIAA Paper 96-2253, New Orleans, LA, June 1996.
9. Liu, T., et al., "Applications of Photogrammetry to Wind Tunnel Testing. Part 1: Camera Calibration Techniques," *Exp. in Fluids*, in preparation.
10. Wong, K. W., "Basic Mathematics of Photogrammetry," in *Manual of Photogrammetry, 4th Ed.,* Slama, C. C., ed. (American Society of Photogrammetry, Falls Church, VA, 1980), Chapter 2.
11. Abdel-Aziz, Y. I. and Karara, H. M., "Direct Linear Transformation from Comparator Coordinates into Object Space Coordinates in Close-Range Photogrammetry," Proc. ASP/UI Symp. on Close-Range Photogrammetry (Univ. of Illinois at Urbana-Champaign, Urbana, IL, 1971), 1-18.
12. Goldstein, H., *Classical Mechanics,* Addison-Wesley, Reading, MA, 1980 , p. 609, 2nd Ed.
13. Caceci, M. S. and Cacheris, W. P., "Fitting Curves to Data," *Byte*, May 1984, pp. 340-362.
14. Sellers, M. E. and Brill, J. A., "Demonstration Test of Pressure Sensitive Paint in the AEDC 16-ft Transonic Wind Tunnel Using the TST model," AIAA Paper 94-2481, Colorado Springs, CO, June 1994.
15. Sellers, M. E., "Pressure Sensitive Paint Data on the Transonic Technology Wing Demonstrator (TST) in the AEDC Propulsion Wind Tunnel 16T," AEDC-TR-98-3, 1998.